



# Hierarchical nano-sized ZnZr-Silicalite-1 multifunctional catalyst for selective conversion of ethanol to butadiene

Kangzhou Wang<sup>a</sup>, Weizhe Gao<sup>a</sup>, Fei Chen<sup>a</sup>, Guangbo Liu<sup>b</sup>, Jinhu Wu<sup>b</sup>, Na Liu<sup>c</sup>, Yugo Kawabata<sup>a</sup>, Xiaoyu Guo<sup>a</sup>, Yingluo He<sup>a,\*</sup>, Peipei Zhang<sup>a,\*</sup>, Guohui Yang<sup>a</sup>, Noritatsu Tsubaki<sup>a,\*</sup>

<sup>a</sup> Department of Applied Chemistry, School of Engineering, University of Toyama, Gofuku 3190, Toyama 930-8555, Japan

<sup>b</sup> Qingdao Institute of Biomass Energy and Bioprocess Technology, Chinese Academy of Science, Qingdao 266101, China

<sup>c</sup> School of Materials Science and Engineering, Central South University of Forestry and Technology, Changsha, Hunan 410004, China

## ARTICLE INFO

### Keywords:

Ethanol  
Butadiene  
Hierarchical structure  
Catalyst activity  
Catalyst stability

## ABSTRACT

Direct conversion of ethanol to butadiene (ETB) is a promising process for the production of renewable butadiene, but it still confronts great obstacles such as low butadiene selectivity and poor stability. Here, we report a hierarchical nano-sized ZnZr-Silicalite-1 multifunctional catalyst with high catalytic performance and stability in direct ETB process, and it was prepared by a facile one-pot crystallization process. The hierarchical nano-sized ZnZr-Silicalite-1 multifunctional catalyst achieved excellent butadiene selectivity of 61.4% and ethanol conversion of 89.8% at 350 °C and 0.38 h<sup>-1</sup>. More importantly, it possessed superior stability compared to the previously reported catalyst systems. The effect of catalyst properties on catalytic performance were investigated using multiple characterized techniques. The results displayed that the ZnZr-Silicalite-1 catalyst possessed a hierarchical nano-sized structure, synergistic effects of various active centers, and suitably balanced acid-base properties. These properties realized excellent catalytic performance and stability for direct ETB conversion.

## 1. Introduction

Butadiene (BD) is an important industrial chemical used as a monomer in the manufacture of synthetic resins, nylon, rubber, etc [1, 2]. Currently, it is predominantly obtained from the byproduct of naphtha cracking to form light olefins [3]. However, the rapid depletion of petroleum reserves and the use of shale gas as a renewable resource for the production of light olefins have led to a remarkable reduction in BD production [4,5]. Therefore, it is highly urgent to develop a cost-effective and sustainable route for BD production from renewable feedstock. With increasing ethanol production as a renewable carbon resource, especially the development of bioethanol production from fermentation of sugars-rich waste and catalytic conversion of syngas to ethanol, the process of direct conversion of ethanol to butadiene (ETB) is becoming a competitive way to alleviate the BD shortage crisis [6,7].

The direct ETB conversion was first developed by Sergei Lebedev at the beginning of the 1920s, and the mechanism has not yet been fully elucidated. Nevertheless, there is a consensus that the main reaction pathway involves five steps (Scheme 1): (1) the formation of

acetaldehyde from the dehydrogenation of ethanol; (2) the acetaldehyde is converted to acetaldol via aldol condensation; (3) the dehydration of acetaldol to crotonaldehyde; (4) the crotonaldehyde and ethanol are transformed into crotyl alcohol via Meerwein-Ponndorf-Verley (MPV) reaction; and (5) the dehydration of crotyl alcohol to form butadiene [8, 9].

Evidently, the direct ETB process is a very complex tandem reaction, and it requires a multifunctional catalyst with active centers for dehydrogenation, aldol condensation, MPV reaction, and dehydration. The basic or redox is an active site for the dehydrogenation of ethanol to acetaldehyde (step 1) [10]. The aldol condensation and MPV reaction occur at Lewis acid sites (LAS) (steps 2 and 4) [11]. The dehydration reaction is relatively easy, and it occurs on silanol groups (steps 3 and 5) [12]. Therefore, the multifunctional catalyst with a suitable balance of active centers is critical for maximizing BD production in the direct ETB process.

Recent reports revealed that the combination of silicalite-supported metal oxide (ZrO<sub>2</sub>, MgO, Y<sub>2</sub>O<sub>3</sub>, or Ta<sub>2</sub>O<sub>5</sub>) with dehydrogenation promoters (Zn, Ag, or Cu) can constitute an effective catalyst for the direct

\* Corresponding authors.

E-mail addresses: [yingluo@eng.u-toyama.ac.jp](mailto:yingluo@eng.u-toyama.ac.jp) (Y. He), [zhangpp@eng.u-toyama.ac.jp](mailto:zhangpp@eng.u-toyama.ac.jp) (P. Zhang), [tsubaki@eng.u-toyama.ac.jp](mailto:tsubaki@eng.u-toyama.ac.jp) (N. Tsubaki).

<https://doi.org/10.1016/j.apcatb.2021.120822>

Received 21 July 2021; Received in revised form 25 September 2021; Accepted 12 October 2021

Available online 14 October 2021

0926-3373/© 2021 Elsevier B.V. All rights reserved.

ETB conversion (Table S1) [13–21]. In contrast, silicalite-supported Ag and  $\text{ZrO}_2$  catalysts demonstrated good catalytic performance, but Ag had a higher cost as a noble metal. Meanwhile, ZnO also displayed the excellent ability of ethanol dehydrogenation [15,16]. The dealuminated beta zeolite and mesoporous silicalite supported  $\text{ZrO}_2$  and ZnO exhibited higher catalytic performance in direct ETB conversion [16,17,20,21]. However, the beta zeolite synthesis required the use of HF and long crystallization time, or needed the cumbersome post-synthetic dealumination and doping metal process [22,23]. The mesoporous silicalite had a high concentration of silanol groups, which caused the side reaction of ethanol dehydration to ethylene and diethyl ether [15]. Importantly, these catalyst systems exhibited poor stability. The development of multifunctional catalysts with excellent activity, selectivity, and particular stability has always been a challenge in the direct ETB process.

The hierarchical nano-sized silicalite-1 is considered to be an excellent catalyst support due to its hierarchical structure, nano-sized particles, and three-dimensional crystalline morphology, and these properties make it have excellent mass transfer efficiency and the ability of resistance coke deposition [24–26]. Hierarchical structured ZSM-5 was investigated for the conversion of methanol to olefins, and hierarchical structure was beneficial in promoting mass transfer efficiency to improve catalyst lifetime [25]. The nano-sized silicalite-1 also exhibited excellent catalytic activity and catalyst stability in Beckmann rearrangement reaction, and these excellent catalytic performances are caused by nano size, improving the ability of resistance against coke deposition [26]. Meanwhile, titanosilicate (TS-1) was intensely investigated for selective oxidation reaction, and the role of hierarchical pores on mass transfer was discussed [27]. The facile one-pot crystallization not only effectively improved the dispersion of active centers but also enhanced the interaction of various active centers on the multifunctional catalyst [28]. In addition, the hierarchical nano-sized structure could enhance the interaction of silicalite-1 and metal oxide to form more active centers [24]. These properties are possibly beneficial to inhibit coke deposition and improve catalytic performance toward BD production in the direct ETB process. Therefore, we present a facile one-pot synthesis of hierarchical nano-sized ZnZr-Silicalite-1 catalyst is feasible for boosting activity and stability in the ETB process. However, to the best of our knowledge, the hierarchical nano-sized catalyst designed for the direct ETB conversion has not yet been explored.

In this work, we report that a hierarchical nano-sized ZnZr-Silicalite-1 multifunctional catalyst was prepared by facial crystallization process, and its catalytic performance and stability for the direct ETB conversion were evaluated. To get a deep insight into the relationship between the chemical properties of catalyst and catalytic performance, we analyzed these catalysts via multiple characterization techniques. The characterization results revealed that the ZnZr-Silicalite-1 multifunctional catalyst possessed a hierarchical nano-sized structure and synergistic effects on each active center. The relationship between the acid-base

properties and BD yield was established. Meanwhile, the hierarchical nano-sized ZnZr-Silicalite-1 catalyst exhibited outstanding catalytic performance and stability for the BD production from ethanol under optimized catalyst preparation parameters and reaction conditions.

## 2. Experimental

### 2.1. Chemicals and materials

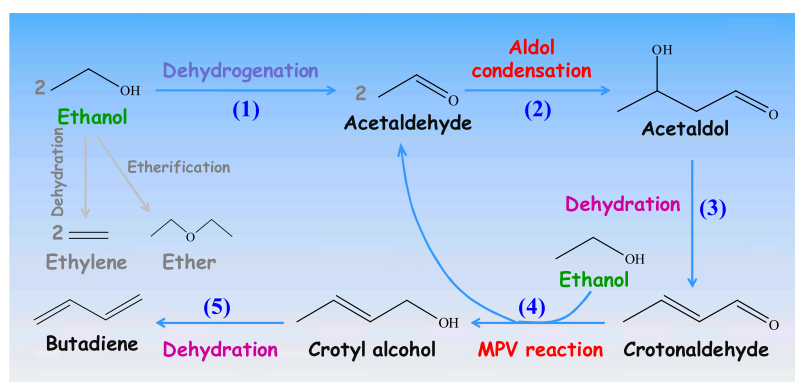
Tetraethyl orthosilicate (TEOS, 99.0%), zinc acetate ( $\text{Zn}(\text{CH}_3\text{COO})_2 \cdot 2\text{H}_2\text{O}$ , 99.0%), n-Hexadecyltrimethylammonium Bromide (CTAB, 99.0%), and ZnO powder were purchased from the Kanto Chemical Co., Inc. Zirconium(IV) butoxide solution ( $\text{Zr}(\text{O}i\text{Bu})_4$ , 80 wt% in 1-butanol) was purchased from the Sigma-Aldrich Co., LLC. Glycerol (99.0%), Ethanol (EtOH, 95.0%) and  $\text{ZrO}_2$  powder were obtained from the Wako Pure Chemical Corporation. Tetrapropylammonium hydroxide (TPAOH, 20–25 wt% in water) was purchased from the Tokyo Chemical Industry Co., Ltd.

### 2.2. Catalyst preparation

The zircon-silicate precursor was prepared by co-precipitation. In brief, CTAB of 1.91 g was dissolved in deionized water of 300 mL under stirring to obtain a solution A. TEOS of 2.60 g and  $\text{Zr}(\text{O}i\text{Bu})_4$  of 2.40 g were mixed in ethanol of 10 mL under stirring to obtain a solution B, and it was slowly added into the solution A under stirring and then aged overnight. The solid products were centrifuged at 2500 rpm and dried overnight at 60 °C to obtain zircon-silicate precursor.

Hierarchical nano-sized ZnZr-Silicalite-1 catalysts were synthesized via hydrothermal synthesis. Typically,  $\text{Zn}(\text{CH}_3\text{COO})_2 \cdot 2\text{H}_2\text{O}$  of 0.05 g and TEOS of 2.60 g were dissolved into EtOH of 10 mL. The above-mentioned zircon-silicate precursor was added into the mixture solution and stirred for 1 h. Then TPAOH of 5.08 g and  $\text{H}_2\text{O}$  of 18.69 g were added drop-wise into the mixture solution under stirring. The mixture solution was continuously stirred at 700 rpm for 4 h, and then heated at 90 °C to remove the most of water and ethanol from the mixture. A gel was formed and subsequently mixed with glycerol of 2.30 g, then transferred into a Teflon-lined stainless steel autoclave for hydrothermal synthesis at 130 °C for 48 h. The product was dried at 100 °C for 12 h, and then calcined at 550 °C in air for 5 h to obtain hierarchical nano-sized  $\text{Zn}_x\text{Zr}_y\text{-S-1}$  catalysts, where x and y represent Zn/Si and Zr/Si molar ratio ( $x = 0.005, 0.01, 0.02, \text{ and } 0.03$ ;  $y = 0.05, 0.2, \text{ and } 0.3$ ), respectively. Among them, when the Zn/Si molar ratio was 0.01, the catalysts with Zr/Si molar ratios of 0.05, 0.2, and 0.3 were labeled as ZnZr-S-1(hn-0.05), ZnZr-S-1(hn-0.2), and ZnZr-S-1(hn-0.3), respectively. The Zr-Silicalite-1 catalyst with Zr/Si molar ratio of 0.2 was also prepared by the same method mentioned above but without the introduction of the ZnO. We denoted this sample with Zr-S-1(hn-0.2).

The hydrothermal synthesis was further employed to synthesize the



Scheme 1. The main reaction pathway of direct ETB reaction.

microporous ZnZr-Silicalite-1 catalyst. The zircon-silicate precursor was not prepared, and the same amounts of  $\text{Zr}(\text{OBU})_4$  and TEOS were added into the mother liquor of Silicalite-1 without adding CTAB and glycerol. The other processes and amounts were the same as those of hierarchical nano-sized ZnZr-S-1(hn-0.2) catalyst. We labeled this sample with ZnZr-S-1(mi-0.2).

### 2.3. Catalyst characterization

The X-ray diffraction (XRD) patterns of the catalysts were carried out using a powder X-ray diffractometer (RINT 2400; Rigaku) with Cu-K $\alpha$  radiation at a scanning speed of  $4^\circ \text{ min}^{-1}$  in the range of  $3\text{--}65^\circ$ .

The elemental composition of the sample was analyzed by Shimadzu Rayn EDX-700 measurement as an energy dispersive X-ray spectrometer.

The nitrogen ( $\text{N}_2$ ) adsorption and desorption measurements of the samples were conducted on a Micromeritics 3Flex 2MP instrument. Prior to the measurements, the catalyst was degassed at  $350^\circ\text{C}$  for 5 h under vacuum conditions. Mesoporosity was defined as the ratio of mesopore volume to total pore volume.

The surface morphologies of the catalysts were observed on a field emission scanning electron microscopy (FE-SEM) using a JEOL JSM-6700F. The high-resolution transmission electron microscopy (HR-TEM) and elemental mapping images were obtained on a JEM-2100F (JEOL) instrument with an acceleration voltage of 200 kV.

Fourier transform infrared resonance (FT-IR) was carried out on an IR Prestige-21 infrared spectrometer with a resolution of  $4 \text{ cm}^{-1}$  and the scanning range from 4000 to  $400 \text{ cm}^{-1}$ .

The X-ray photoelectron spectroscopy (XPS) analysis was performed on a Thermo Fisher Scientific ESCALAB 250Xi instrument with an Al K $\alpha$  X-ray radiation source. All binding energy was calibrated to the Si 2p line at 103.4 eV.

$^{29}\text{Si}$  solid-state cross-polarization magic angle spinning nuclear magnetic resonance ( $^{29}\text{Si}$  CP MAS NMR) was performed on a JEOL RESONANCE JNM-ECX500 spectrometer. The spectra were obtained with a resonance frequency of 99.4 MHz, the repetition time of 15.4 s, and the sample spinning rate of 19.8 kHz.

The acid properties of the catalyst were studied by temperature-programmed desorption of ammonia ( $\text{NH}_3$ -TPD) on a BELCAT-II-T-SP apparatus. In brief, the sample of 0.05 g was loaded into a quartz tube and pretreated under flowing helium ( $30 \text{ mL min}^{-1}$ ) at  $400^\circ\text{C}$  for 1 h and then cooled to  $80^\circ\text{C}$ . Then the catalyst was saturated with  $\text{NH}_3$  at  $80^\circ\text{C}$  for 1 h using an  $\text{NH}_3/\text{He}$  mixture (5 vol%  $\text{NH}_3$ ), followed by purging weak adsorption  $\text{NH}_3$  under flowing helium gas for 1 h.  $\text{NH}_3$  desorption was analyzed using a thermal conductivity detector (TCD) at the temperature from  $80^\circ$  to  $650^\circ\text{C}$  at a rate of  $10^\circ\text{C min}^{-1}$ .

The acid type of the sample was investigated by pyridine adsorption infrared spectroscopy (Py-IR) using a Bruker Tensor 27 device attached to an in situ cell. The sample was packed into the cell and pretreated at  $400^\circ\text{C}$  for 1 h under a vacuum, followed by the sample cooled down to  $100^\circ\text{C}$  and a reference spectrum was recorded. Afterward, the pyridine vapor was introduced into the cell at  $100^\circ\text{C}$  for 10 min and retained for 30 min. After reaching equilibrium, the pyridine-adsorbed system was heated and conducted at  $150^\circ\text{C}$ , and then the spectra were recorded. The acid amount was calculated by the following equations:  $C = (\text{IA} \times S)/(\text{W} \times \text{IMEC})$ , where  $C$  – acid amount ( $\mu\text{mol g}^{-1}$ ),  $\text{IA}$  – integrated absorbance of LAS bands ( $\text{cm}^{-1}$ ),  $S$  – the surface area of sample wafer ( $1.325 \text{ cm}^2$ ),  $W$  – sample weight, and  $\text{IMEC}$  – integrated molar extinction coefficient of LAS ( $2.22 \text{ cm } \mu\text{mol}^{-1}$ ) [29].

The basicity of the catalyst was determined by temperature-programmed desorption of carbon dioxide ( $\text{CO}_2$ -TPD) also using the BELCAT-II-T-SP instrument. Typically, the sample of 0.05 g was placed into a quartz tube and pretreated at  $200^\circ\text{C}$  for 1 h under flowing helium gas ( $30 \text{ mL min}^{-1}$ ). After the sample was cooled down to  $50^\circ\text{C}$ ,  $\text{CO}_2$  was purged into the quartz tube for 30 min. Subsequently, the weak adsorption of  $\text{CO}_2$  was removed with flowing helium gas for 1 h. The

$\text{CO}_2$  desorption was performed with the temperature from  $50^\circ\text{C}$  to  $650^\circ\text{C}$  with a rate of  $10^\circ\text{C min}^{-1}$ .

Thermogravimetric (TG) analysis of the spent catalyst was performed on a Shimadzu DTG-60 thermal analyzer, and the sample was heated from  $30^\circ\text{C}$  to  $600^\circ\text{C}$  with a ramping rate of  $10^\circ\text{C min}^{-1}$  under air atmosphere.

The temperature-programmed diffuse reflectance infrared Fourier transform spectroscopy (TP-DRIFTS) analysis was performed on a Thermo Nicolet (NEXUS-470) FTIR spectrometer equipped with liquid nitrogen cooled high sensitivity MCT detector and high-temperature in situ chamber. In brief, the catalyst powder was placed in the chamber. Prior to the reaction, the catalyst was pretreated under helium gas flow ( $10 \text{ mL min}^{-1}$ ) at  $450^\circ\text{C}$  for 1 h. Subsequently, the catalyst was cooled to  $30^\circ\text{C}$  for recording the background spectra. Then, a saturated vapor of ethanol was fed into the chamber, and the spectra were recorded with a resolution of  $4 \text{ cm}^{-1}$  and an accumulation of 32 scans by raising the temperature from  $30^\circ$  to  $450^\circ\text{C}$ .

Ethanol temperature-programmed surface reaction (TPSR) was carried out on a fixed-bed microreactor connected to Hidden QGA Quantitative Gas Analysis System (Hidden Analytical). In brief, the catalyst of 0.05 g was placed into microreactor and pretreated at  $450^\circ\text{C}$  for 1 h under flowing helium gas ( $20 \text{ mL min}^{-1}$ ), then the sample was cooled down to  $30^\circ\text{C}$ , and a saturated vapor of ethanol was fed into the quartz tube using the helium gas as carrier gas for 30 min. Then, the temperature-programmed heating from  $30^\circ$  to  $500^\circ\text{C}$  with a rate of  $5^\circ\text{C min}^{-1}$  simultaneously with mass spectrometer analysis of the products was performed. The ethanol and main intermediates were analyzed with the corresponding mass-to-charge ( $m/z$ ) signals: ethanol ( $\text{C}_2\text{H}_5\text{OH}$ , 46), water ( $\text{H}_2\text{O}$ , 18), hydrogen ( $\text{H}_2$ , 2), acetaldehyde ( $\text{C}_2\text{H}_4\text{O}$ , 44), acetaldol ( $\text{C}_4\text{H}_8\text{O}_2$ , 88), crotonaldehyde ( $\text{C}_4\text{H}_6\text{O}$ , 70), crotyl alcohol ( $\text{C}_4\text{H}_8\text{O}$ , 72), and butadiene ( $\text{C}_4\text{H}_6$ , 54).

### 2.4. Catalytic evaluation

The direct ETB reaction was performed in a fixed-bed reactor at atmospheric pressure. Typically, the catalyst of 0.5 g was loaded into the reactor and pretreated under flowing nitrogen ( $20 \text{ mL min}^{-1}$ ) at  $450^\circ\text{C}$  for 1 h. Then, the catalyst was cooled down to reaction temperature, and the ethanol (95% aqueous ethanol) was introduced into the system using a syringe pump and  $\text{N}_2$  as carrier gas flow of  $20 \text{ mL min}^{-1}$  at a weight hourly space velocity ( $\text{WHSV}$ ) =  $0.19\text{--}1.89 \text{ h}^{-1}$  for ethanol only. The catalytic reaction was evaluated for 6 h of time-on-stream (TOS), and the products were analyzed by on-line gas chromatograph (GC) Shimadzu GC-14B with flame ionization detector (FID) and DB-1 capillary column ( $30 \text{ m} \times 0.25 \text{ mm} \times 0.25 \mu\text{m}$ ), and it was used to analyze ethylene, ethane, butadiene, ethanol, acetaldehyde, diethyl ether, and other products (others include minor amounts of by-products, such as methane, ethane, propane, propene, acetone,  $\text{C}_4$  and  $\text{C}_6+$  compounds). The stability of ZnZr-S-1(mi-0.2) and ZnZr-S-1(hn-0.2) catalysts was measured under optimized reaction conditions. The reaction was continued for 80 h of TOS, and the products were intermittently analyzed by on-line GC with an interval of 12 h.

Results were calculated as:

$$X_{\text{EtOH}} (\%) = (n_{\text{EtOH},\text{in}} - n_{\text{EtOH},\text{out}}) / n_{\text{EtOH},\text{in}} \times 100 \quad (1)$$

$$S_i (\%) = A_i f_i / \sum A_i f_i \times 100 \quad (2)$$

$$\text{BD yield} (\%) = X_{\text{EtOH}} \times S_{\text{BD}} \times 100 \quad (3)$$

Where  $X_{\text{EtOH}}$  – ethanol conversion;  $n_{\text{EtOH},\text{in}}$  – mole number of ethanol in feedstock;  $n_{\text{EtOH},\text{out}}$  – mole number of ethanol in reaction products;  $S_i$  – selectivity of product  $i$ ;  $A_i$  – peak area of product  $i$ ;  $f_i$  – correction factor from product  $i$ ;  $S_{\text{BD}}$  – the selectivity of butadiene.

### 3. Results and discussion

#### 3.1. Structural characterization

All catalysts exhibited the typical XRD peaks of MFI-type zeolite at  $8.0^\circ$ ,  $8.9^\circ$ ,  $23.2^\circ$ ,  $23.9^\circ$ , and  $24.3^\circ$ , but any characteristic peaks of bulk ZnO and ZrO<sub>2</sub> were not observed (Fig. S1), suggesting that the metal oxides particles were dispersed on silicalite-1 or the crystal sizes of ZnO and ZrO<sub>2</sub> species was lower than the detection limitation of XRD. In addition, the intensity of the ZnZr-S-1(hn-0.2) and ZnZr-S-1(hn-0.3) diffraction peaks decreased compared to that of ZnZr-S-1(hn-0.05), indicating that Zr species were incorporated into the framework of silicalite-1 [30]. Meanwhile, the results of the EDX spectrometer revealed that the elemental composition of catalysts was similar to their theoretical value (Table S2).

To reveal the textural properties, the catalysts were analyzed by N<sub>2</sub> adsorption-desorption. ZnZr-S-1(mi-0.2) displayed only unimodal, while other catalysts exhibited bimodal structure (Fig. S2). This result revealed that ZnZr-S-1(hn)-based catalysts possessed the expected hierarchical structure. The textural properties were summarized in Table 1. ZnZr-S-1(mi-0.2) exhibited a large specific surface area of 518 m<sup>2</sup> g<sup>-1</sup>, but a much smaller pore volume and very small pore diameter. In contrast, the hierarchical ZnZr-S-1(hn)-based catalysts displayed high mesopore volume and mesoporosity, especially the large pore diameter. Compared with Zr-S-1(hn-0.2), the mesopore diameter and volume of ZnZr-S-1(hn-0.2) increased, and the micropore properties and specific surface areas did not change. With increasing the Zr/Si molar ratio, the specific surface areas, mesopore volume, and diameter increased until reaching a maximum and then decreased, since Zr species were first incorporated into the framework to reach the maximum, and then formed the metal oxides in the pore [31,32]. Among them, ZnZr-S-1(hn-0.2) displayed a large pore volume of 0.63 cm<sup>3</sup> g<sup>-1</sup> (vs. 0.44 cm<sup>3</sup> g<sup>-1</sup>), mesopore diameter of 7.46 nm (vs. 2.78 nm) and micropore diameter of 0.71 nm (vs. 0.28 nm) as well as maximum mesoporosity of 88.9% compared to that of ZnZr-S-1(mi-0.2). In addition, the distribution of mesopore was relatively wide (Fig. S2). These properties were beneficial to improve mass transfer efficiency.

The morphologies and crystal sizes of catalysts were unveiled by SEM and TEM analyses. ZnZr-S-1(mi-0.2) consisted of rectangular particles of different sizes (Fig. 1b). However, Zr-S-1(hn-0.2) and ZnZr-S-1(hn-0.2) were mainly composed of nano-sized particles (about 150 nm) (Fig. 1a and c). The particle size of ZnZr-S-1(hn-0.2) was smaller than that of ZnZr-S-1(mi-0.2) (Fig. S3). The TEM images of ZnZr-S-1(mi-0.2) and ZnZr-S-1(hn-0.2) further revealed that ZnZr-S-1(hn-0.2) had nanometer size (Fig. 4d–f). In Fig. 4g, it can be seen that Zn and Zr closely combined with silicalite-1. Meanwhile, the elemental mapping of ZnZr-S-1(mi-0.1) and ZnZr-S-1(hn-0.2) further indicated that the Zn and Zr species were uniformly dispersed on the silicalite-1 (Figs. 1h and S4). These results combined with the texture properties further demonstrated that hierarchical nano-sized ZnZr-S-1(hn)-based catalysts were successfully

achieved by a crystallization process from amorphous phases into zeolite crystalline structure.

FT-IR spectra were used to explore the existence and function of typical functional group. In Fig. 2a, two bands were observed at 1076 cm<sup>-1</sup> and 1226 cm<sup>-1</sup>, which belong to the typical asymmetric stretching vibrations of Si—O—Si bonds [33]. Bands at 796 and 450 cm<sup>-1</sup> were due to symmetric stretching and rocking vibrations of Si—O—Si bonds, respectively [33]. The band at 550 cm<sup>-1</sup> was attributed to the double-ring tetrahedral vibration in the silicalite-1 framework, whereas this band was split into two bands in the ZnZr-S-1(hn-0.2) catalysts, and it was caused by the vibrations of double five-membered ring [34]. This finding further verified that the ZnZr-S-1-based catalyst was successfully synthesized and possessed a nanometer size [34]. The band at 1076 cm<sup>-1</sup> shifted to high wave-number compared to that of silicalite-1, and it was broadened and overlapped with each other, owing to the fact that the strong interaction between of Zr species and Si species to form Si—O—Zr band [33].

To further verify the interaction, XPS and <sup>29</sup>Si solid-state MAS NMR analysis were conducted for the catalysts. The C 1s peak is often used as an internal standard for the calibration of the binding energy in powder samples such as heterogeneous catalyst. Recent studies have found that the calibration procedure based on the C 1s peak of the adventitious carbon is highly arbitrary, which results in incorrect interpretation of the spectra [35,36]. Here, we choose the Si 2p peak at 103.4 eV as the internal standard to calibrate the binding energy [37]. In Fig. 2b, one peak at 103.4 eV was observed on silicalite-1. Compared with reference silicalite-1, the Si 2p peak of synthesized catalysts was obviously broadened. When the Zr/Si molar ratio increased above 0.2, a weak shoulder peak appeared. The Zn 2p peaks of synthesized catalysts appeared at 1046.4 eV and 1023.1 eV, respectively (Fig. S5). Two shoulder peaks were observed in the Zr 3d peaks of the synthesized catalysts (Fig. S6). In addition, the O 1s peak of synthesized catalysts also appeared with an obvious shoulder peak at 530.7 eV (Fig. 2c). These shoulder peaks were assigned to the Si—O—Zr bonds [38–40]. Compared with ZnZr-S-1(mi-0.2), ZnZr-S-1(hn-0.2) displayed stronger shoulder peak. This result indicated that the hierarchical nano-sized structure enhanced the interaction between metal and silanol, and it also facilitated the formation of more active centers to improve BD production.

In Fig. 2d, <sup>29</sup>Si MAS NMR spectra of three samples exhibited a main resonance at -112 ppm, which was attributed to Si(OSi)<sub>4</sub> (Q<sup>4</sup> unit) coordination [41]. Compared with reference silicalite-1, both ZnZr-S-1(mi-0.2) and ZnZr-S-1(hn-0.2) samples displayed a weak shoulder peak at -102 ppm, which was assigned to Si(OSi)<sub>3</sub>OH or Si(OSi)<sub>3</sub>(OZr) (Q<sup>3</sup> unit) coordination, and this weak shoulder peak was mainly caused by the distorted silicon environment in tetrahedral due to Si—O—Zr bond [42]. This result further revealed the interaction between Zr species and silanol to formation Si—O—Zr bonds. However, ZnZr-S-1(mi-0.2) displayed a weak shoulder peak at -92 ppm, which was attributed to Si(OSi)<sub>2</sub>(OH)<sub>2</sub> (Q<sup>2</sup> unit) coordination, but this shoulder

**Table 1**  
Textural properties of the synthesized catalysts.

Samples	A <sub>BET</sub> <sup>a</sup> (m <sup>2</sup> g <sup>-1</sup> )	V <sub>micro</sub> <sup>b</sup> (cm <sup>3</sup> g <sup>-1</sup> )	V <sub>meso</sub> <sup>c</sup> (cm <sup>3</sup> g <sup>-1</sup> )	V <sub>total</sub>	D <sub>micro</sub> <sup>d</sup> (nm)	D <sub>meso</sub> <sup>e</sup> (nm)	Mesoporosity <sup>f</sup> (%)
Zr-S-1(hn-0.2)	298	0.08	0.43	0.51	0.71	5.72	84.3
ZnZr-S-1(mi-0.2)	518	0.08	0.36	0.44	0.28	2.78	81.8
ZnZr-S-1(hn-0.05)	290	0.08	0.44	0.52	0.62	6.04	84.6
ZnZr-S-1(hn-0.2)	300	0.07	0.56	0.63	0.71	7.46	88.9
ZnZr-S-1(hn-0.3)	295	0.07	0.45	0.52	0.75	6.05	86.5

<sup>a</sup> BET surface area;

<sup>b</sup> micropore volume calculated by t-plot method;

<sup>c</sup> mesopore volume calculated by BJH method;

<sup>d</sup> average diameter for micropores evaluated by HK method;

<sup>e</sup> average diameter of mesopores evaluated by the BJH method.

<sup>f</sup> mesoporosity was calculated via the ratio of mesopore volume to total pore volume.



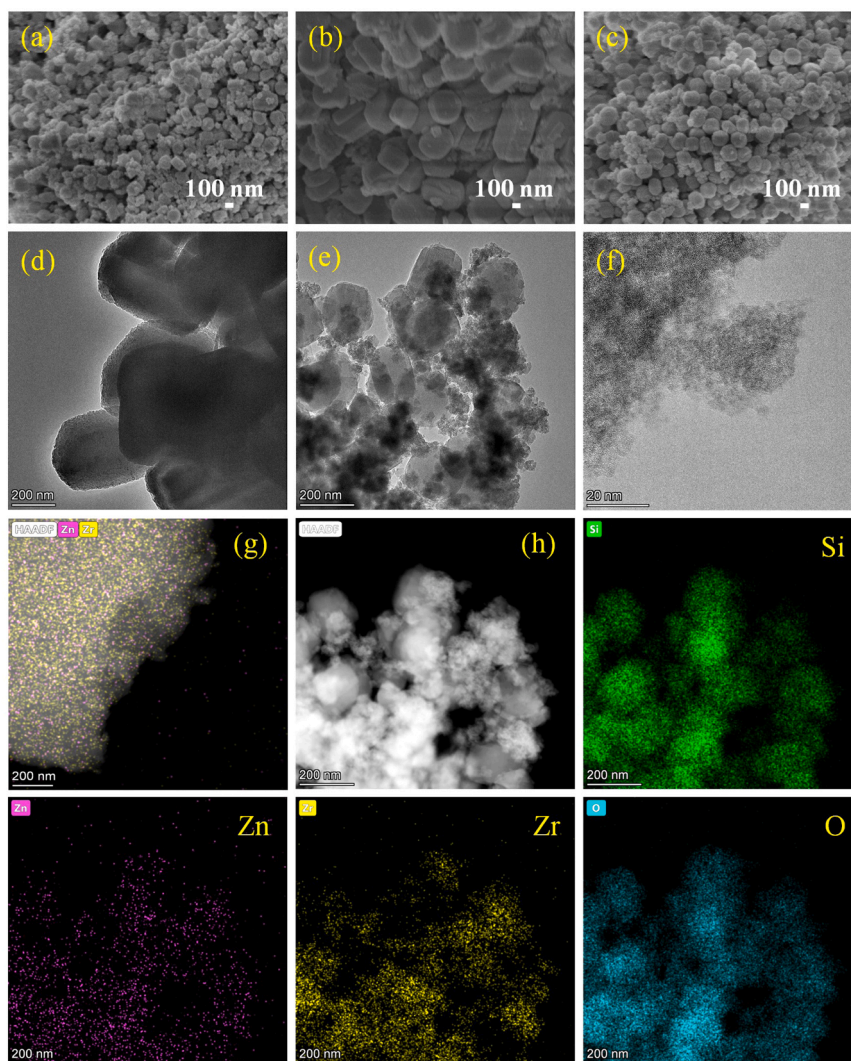


**Fig. 1.** SEM images of the catalysts (a) Zr-S-1(hn-0.2), (b) ZnZr-S-1(mi-0.2), and (c) ZnZr-S-1(hn-0.2), TEM images of the catalyst (d) ZnZr-S-1(mi-0.2) and (e, f) ZnZr-S-1(hn-0.2), (g) the image of STEM and Zn, Zr mapping of ZnZr-S-1(hn-0.2) catalyst, (h) STEM image of ZnZr-S-1(hn-0.2), and elemental mapping images from STEM-EDS analysis for the ZnZr-S-1(hn-0.2) catalyst.

peak was not detected in ZnZr-S-1(hn-0.2). This result indicated that ZnZr-S-1(hn-0.2) had much lower hydroxyl groups, which could inhibit the side reaction of ethanol dehydration to ethylene [43].

### 3.2. Acid-base properties

The acid properties of the catalysts were measured by  $\text{NH}_3$ -TPD. It was clearly found that the silicalite-1 had lower acid properties, while other catalysts exhibited strong desorption peaks (Fig. S7). Zr-S-1(hn-0.2) displayed desorption peaks center at 155 °C and 415 °C, corresponding to the weak acid and strong acid sites, respectively. ZnZr-S-1-based catalysts exhibited the weak acid peak being shifted to a higher temperature while the strong acid peak shifted to a lower temperature compared to those of Zr-S-1(hn-0.2), indicated that the strength of weak acid increased and the strength of strong acid decreased. In Table 2, ZnZr-S-1(hn-0.2) has a higher acid amounts compared to that of Zr-S-1(hn-0.2). Meanwhile, the total acid amount and the ratio of strong acid to total acid also increased with increasing the Zr/Si molar ratio. Compared with ZnZr-S-1(hn-0.2), the strong acid amount of ZnZr-S-1(mi-0.2) decreased, while the weak acid amount and the ratio of strong acid to total acid increased, because the weak acid of ZnZr-S-1(mi-0.2) is mainly derived from the silanol groups. These results

further implied that the hierarchical nano-sized structure effectively enhanced the interaction between metal oxides and silicalite-1 to form more strong acid [44].

To further investigate and characterize the type of acid sites, we analyzed the pyridine adsorption FT-IR and the results were exhibited in Fig. 3. The bands at 1442, 1578, 1595, and 1607  $\text{cm}^{-1}$  are contributed to pyridine coordinative bound to LAS, and the band at 1485  $\text{cm}^{-1}$  are assigned to the pyridine bonded to LAS and Brønsted acid sites (BAS) [45,46]. BAS was not detected in all catalysts. However, the bands at 1578 and 1595  $\text{cm}^{-1}$  were observed in ZnZr-S-1(hn-0.2), but these two bands did not appear in ZnZr-S-1(mi-0.2), since LAS of ZnZr-S-1(hn-0.2) was mainly derived from the Zn and Zr species interacting with silanol groups. The reason for this result is that the zircon-silicate precursor used in the ZnZr-S-1(hn-0.2) synthesis process could enhance the interaction of Zn and Zr species with silanol groups [40]. The bands of ZnZr-S-1(hn-0.2) shifted to lower wavenumber compared to those of ZnZr-S-1(mi-0.2), owing to the fact that Zr species generated weaker LAS than Zn species owing to the weaker electronegativity of the former metal [47]. This result is consistent with the acid strength of  $\text{NH}_3$ -TPD (Table 2). The LAS amounts were listed in Table 2. ZnZr-S-1(hn-0.2) generated a higher amount of LAS than that of ZnZr-S-1(mi-0.2), but  $\text{NH}_3$ -TPD exhibited that ZnZr-S-1(mi-0.2) had a higher acid amount

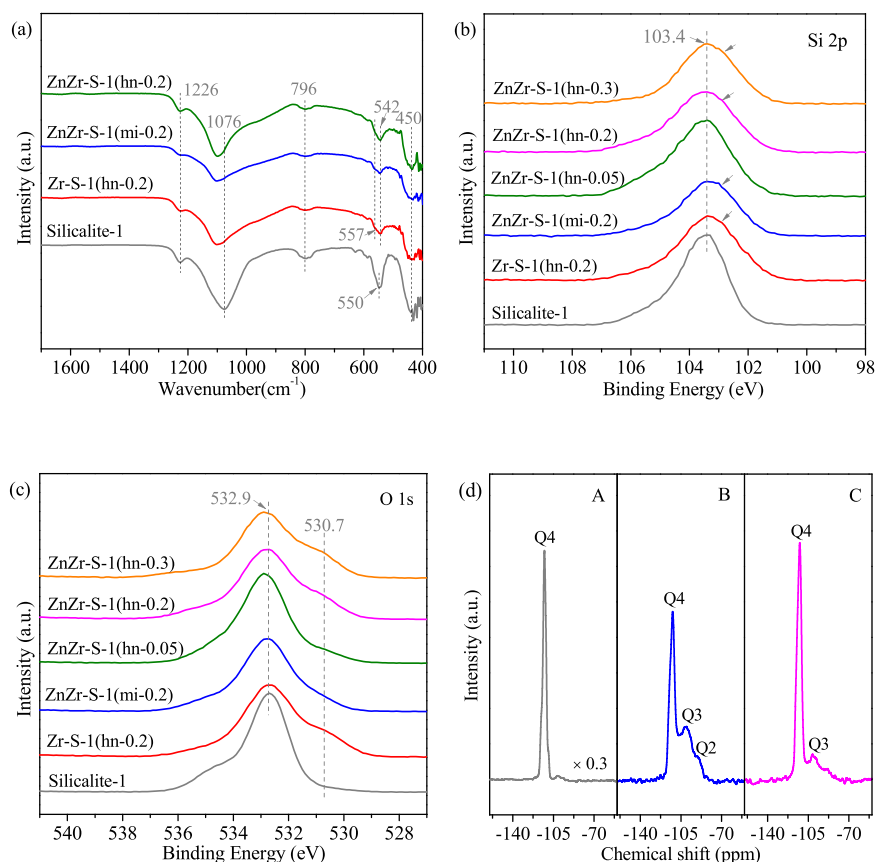


**Fig. 2.** Characterization of active centers interaction. (a) FT-IR spectra of the silicalite-1 and synthesized catalysts; (b) Si 2p XPS spectra of the silicalite-1 and synthesized catalysts; (c) O 1s XPS spectra of the silicalite-1 and synthesized catalysts; (d)  $^{29}\text{Si}$  MAS NMR spectra of (A) silicalite-1, (B) ZnZr-S-1(mi-0.2), and (C) ZnZr-S-1(hn-0.2).

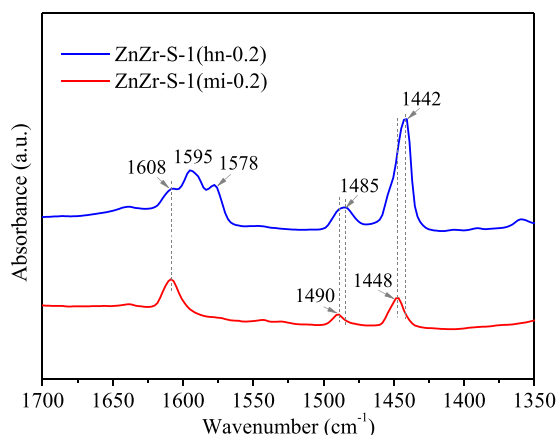


**Fig. 3.** FT-IR spectra of adsorbed pyridine on catalysts after desorption at 150 °C.

compared to that of ZnZr-S-1(hn-0.2), especially weak acid amount (Table 2). This result indicated that ZnZr-S-1(mi-0.2) had more Si-OH groups in silanol nests, which had weak acid properties [48]. However, ZnZr-S-1(hn-0.2) possessed weaker LAS, which promoted aldol condensation and MPV reaction [49,50].

The base properties of the catalysts were measured by  $\text{CO}_2$ -TPD. The silicalite-1 had low base properties, while Zr-S-1(hn-0.2) presented two peaks at 133 °C and 297 °C, and these are assigned to the weak base sites and strong base sites, respectively (Fig. S8). Compared with Zr-S-1(hn-0.2), with the introduction of Zn species, the weak base and strong

base peaks shifted to high temperature indicated that the strength of basic sites was enhanced by introducing the Zn species. The base amounts were listed in Table 3. Zr-S-1(hn-0.2) had lower base amounts, while ZnZr-S-1(mi-0.2) displayed a maximum value of base amount. Compared with ZnZr-S-1(mi-0.2), the strong base amount and the ratio of strong base to total base of ZnZr-S-1(hn-0.2) decreased, while the weak base amount did not obviously change. With increasing the Zr/Si molar ratio, the strong base amount increased and the weak base amount first increased and then decreased. In contrast, ZnZr-S-1(hn-0.2) exhibited the lowest ratio of strong base to total base. These results revealed that the acid-base properties could be effectively modified via Zn and Zr species [50,51].

### 3.3. Catalytic performance

The catalytic performances of the synthesized catalysts for the direct ETB conversion were studied, and the results were compared in Fig. 4a. Zr-S-1(hn-0.2) exhibited low ethanol conversion and the selectivity of acetaldehyde and BD, and high selectivity of ethylene and diethyl ether, indicated that it possessed strong dehydration ability and lack the activity of ethanol dehydrogenation [52]. When the introduction of Zn species, the ethanol conversion and BD selectivity were significantly increased, demonstrated that Zn species played a critical role in the direct ETB process. ZnZr-S-1(mi-0.2) displayed lower BD selectivity of 38.7% and higher selectivity of others, and the others were formed by the cross-aldol condensation of acetaldehyde and crotonaldehyde, followed by the reduction and dehydration into heavier byproducts [53]. This effect is possibly explained by the fact that micropores inhibited diffusion of formed acetaldehyde, which initiated secondary reactions with unstable crotonaldehyde intermediate to form heavier byproducts

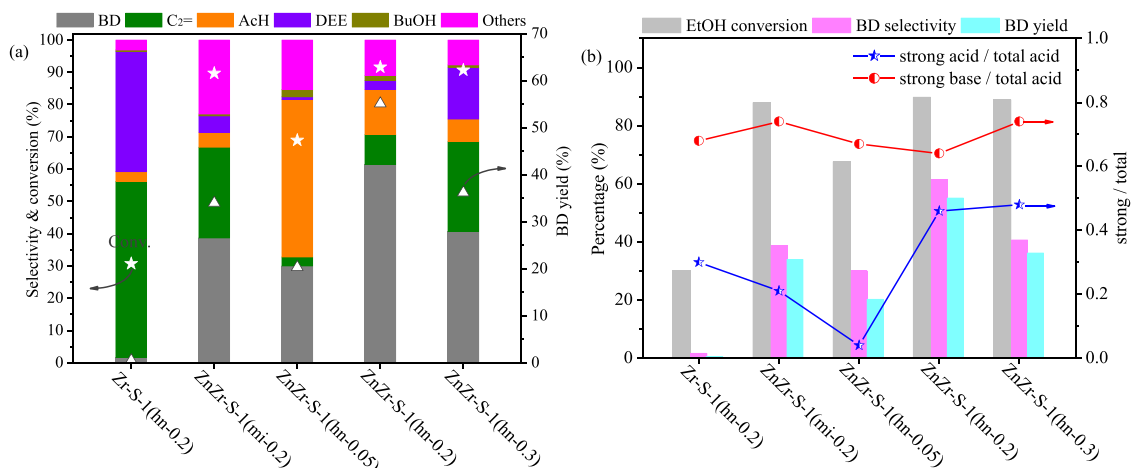


**Fig. 4.** (a) Catalytic performance of the ETB reaction over the synthesized catalysts, (Reaction conditions: catalyst = 0.5 g, T = 350 °C, WHSV = 0.38 h<sup>-1</sup>, and TOS = 6 h. The ethanol, butadiene, ethylene, acetaldehyde, diethyl ether, and 1-butanol was abbreviated as EtOH, BD, C<sub>2</sub>=, AcH, DEE, and BuOH, respectively.) (b) Effect of the ratio of strong acid amount to total acid amount on ethanol conversion, BD selectivity, and BD yield, respectively, and the effect of the ratio of strong base amount to total base amount on ethanol conversion, BD selectivity, and BD yield, respectively. Percentage of y-axis means ethanol conversion, BD selectivity, or BD yield in mole.

**Table 2**

The acidity of the synthesized catalysts.

Samples	Peak position (°C)		Acid amount <sup>a</sup> (mmol g <sup>-1</sup> )				LAS amount (μmol g <sup>-1</sup> ) <sup>b</sup>
	weak	strong	weak	strong	total	strong/total	
Zr-S-1(hn-0.2)	155	415	0.21	0.09	0.30	0.30	/
ZnZr-S-1(mi-0.2)	163	405	0.41	0.11	0.52	0.21	119.8
ZnZr-S-1(hn-0.05)	160	411	0.22	0.01	0.23	0.04	/
ZnZr-S-1(hn-0.2)	162	385	0.25	0.21	0.46	0.46	484.0
ZnZr-S-1(hn-0.3)	164	379	0.33	0.30	0.63	0.48	/

<sup>a</sup> Acid amount was obtained from NH<sub>3</sub>-TPD.

<sup>b</sup> The amount of Lewis acid sites (LAS) was obtained from pyridine-adsorption FT-IR at 150 °C.

**Table 3**

The basic of the synthesized catalysts.

Samples	Peak position (°C)		Base amount (mmol g <sup>-1</sup> ) <sup>a</sup>			
	weak	strong	weak	strong	total	strong/total
Zr-S-1(hn-0.2)	133	297	0.17	0.36	0.53	0.68
ZnZr-S-1(mi-0.2)	150	316	0.22	0.63	0.85	0.74
ZnZr-S-1(hn-0.05)	134	334	0.18	0.37	0.55	0.67
ZnZr-S-1(hn-0.2)	138	328	0.22	0.40	0.62	0.64
ZnZr-S-1(hn-0.3)	141	299	0.17	0.48	0.65	0.74

<sup>a</sup> Base amount was obtained from CO<sub>2</sub>-TPD.

[53]. With the Zr/Si molar ratio increased, the selectivity of BD first increased and then decreased, and the selectivity of ethylene and diethyl ether constantly increased, while the selectivity of acetaldehyde gradually decreased. In contrast, on the ZnZr-S-1(hn-0.2), the BD selectivity reached as high as 61.4% and the ethanol conversion of 89.8%.

The above results proved that a small amount of Zn species had a significant effect on the catalytic performance. To get excellent catalytic performance, we further optimized the Zn/Si molar ratio. The results exhibited that high selectivity of acetaldehyde was achieved at a higher Zn/Si molar ratio. When the Zn/Si molar ratio increased to 0.01, the BD selectivity reached a maximum value of 61.4% (Table S3). The catalytic performance of pure ZnO, ZrO<sub>2</sub>, and silicalite-1 samples were also evaluated (Table S4). The results uncovered that pure ZnO and ZrO<sub>2</sub> had very low ethanol conversion and BD selectivity, and higher selectivity of byproducts, such as ethylene, acetaldehyde, or diethyl ether. The silicalite-1 displayed much low ethanol conversion, without BD production, while a large amount of ethylene and acetaldehyde were

obtained. Therefore, the interaction and synergies among ZnO, ZrO<sub>2</sub>, and silicalite-1 in ZnZr-S-1(hn-0.2) efficiently oriented each step of the direct ETB process to improve the ethanol conversion and BD selectivity.

Many studies have reported that the acid-base properties of the catalysts have a significant influence on catalytic performance in direct ETB conversion [36,43]. To better design the catalyst to maximize the ethanol conversion towards BD production, we have established the relationship between acid-base properties and catalytic performance. As depicted in Fig. 4b, a high BD yield of 55.1% was obtained on the ZnZr-S-1(hn-0.2) catalyst with a moderate ratio of strong acid to total acid of 0.46 and a low ratio of strong base to total base of 0.64. This result indicated that a suitable amount of strong acid and a low amount of strong base were beneficial to the ethanol conversion toward BD production [37,54]. Based on these results, we could deduce that a suitable ratio of strong acid to total acid possessed higher activity for aldol condensation, thus leading to a higher BD yield for direct ETB conversion. Meanwhile, it is observed that the ZnZr-S-1(mi-0.2) exhibited lower BD yield and higher selectivity of ethylene, because more weak acid was beneficial to the formation of ethylene [55]. These results revealed that an appropriate strong acid amount and lower strong base amount led to a balance of each tandem step, being necessary to achieve high BD yield.

### 3.4. Effects of reaction conditions on catalytic performance of the direct ETB process

The direct ETB process consists of tandem steps with different activation energies, the reaction conditions will drastically affect the rate of the rate-determining step. To further enhance the catalytic performance

of our developed catalyst, we further optimized the reaction conditions and the results were compared in Fig. 5. In Fig. 5a, with increasing reaction temperature, the ethanol conversion constantly increased and BD selectivity increased to a maximum value of 61.4% at 350 °C and then gradually decreased. In addition, the acetaldehyde selectivity declined, while the selectivity of others obviously increased, owing to the fact that the cross-aldol condensation of acetaldehyde and crotonaldehyde is more likely to occur above 375 °C, followed by the reduction and dehydration into heavier byproducts [15,56]. In contrast, BD yield could reach a maximum value of 55.1% at 350 °C (Table S5).

The effect of WHSV on catalytic performance has also been investigated on the ZnZr-S-1(hn-0.2) catalyst. In Fig. 5b, with increasing the WHSV, the ethanol conversion, the selectivity of ethylene and others declined, while the acetaldehyde selectivity obviously increased, owing to the fact that the aldol condensation required lower WHSV in this consecutive reaction sequence [57]. In addition, BD selectivity had a maximum value of 61.4% at WHSV of 0.38 h<sup>-1</sup> (Table S6). Considering the butadiene selectivity, the best WHSV of 0.38 h<sup>-1</sup> as the optimized recipe was selected.

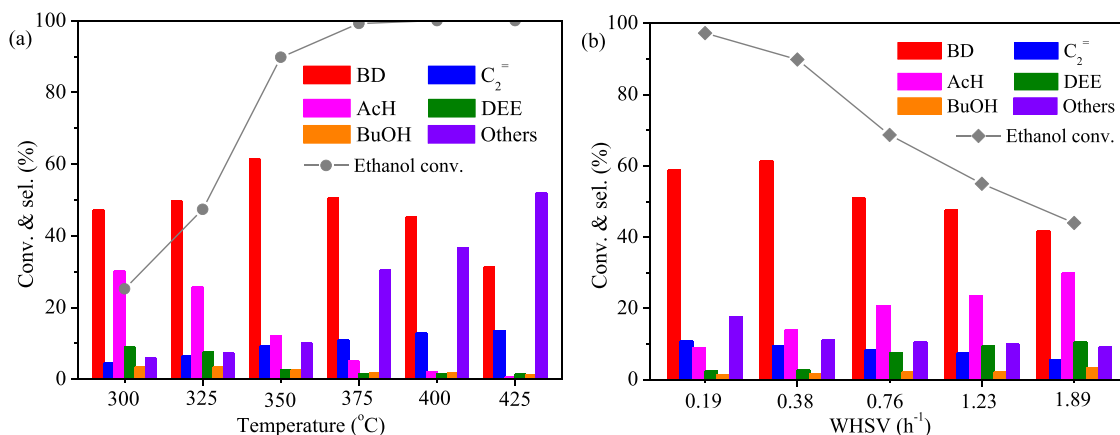
### 3.5. Investigating the rate-determining steps

In the tandem reaction, it is important to investigate the rate-determining steps for better balance the acid-base to maximize the production of BD, we analyzed TP-DRIFTS on ZnZr-S-1(hn-0.2) catalyst and the results were exhibited in Fig. 6a. Two bands were observed at 3734 and 3674 cm<sup>-1</sup>, which hinted at an interaction of ethanol with the Zn-OH and Zr-OH groups [8]. Bands at 2983, 2930, and 2875 cm<sup>-1</sup> were due to CH<sub>3v(a)</sub>, CH<sub>2v(a)</sub>, and CH<sub>3v(s)</sub> stretching modes of ethanol molecules [8,9]. Band at low wavenumber at 1280 cm<sup>-1</sup> was attributed to ethanol molecules coordinated at LAS [8]. According to previous study, the band at 1592 cm<sup>-1</sup> was assigned to C=C vibration modes of ethylene during the initial period, and the band intensity increased with increasing the temperature, suggesting that this band also included the C=C vibration modes of coupling products formed, such as crotyl alcohol and other intermediates [8,17]. With increasing reaction temperature to 200 °C, a new peak appeared at 1688 cm<sup>-1</sup>, and it was assigned to the C=O stretch of acetaldehyde produced by the dehydrogenation of ethanol [15]. Simultaneously, a new band at 1448 cm<sup>-1</sup> was observed at 300 °C, which was attributed to the O—C—O asymmetric and symmetric vibrations of acetate species and crotonaldehyde, and these products were formed via a Cannizzaro reaction of acetaldehyde and the dehydration of acetaldehyde, respectively [58,59]. This result indicated that the generated acetaldehyde could be rapidly involved in the subsequent aldol condensation reaction, thus acetaldehyde was

regarded as the initial intermediate. The dehydrogenation of ethanol to acetaldehyde was relatively easy to proceed. However, the acetaldehyde was not detected during the entire process, suggesting that trace intermediates was further rapidly transformed to subsequent intermediates or desorbed. Based on above reaction conditions analysis, when the ethanol flow ratio was increased, the BD selectivity decreased while the selectivity of acetaldehyde increased, indicated the acetaldehyde accumulation with the contact time decreased (Fig. 5b). The selectivity of acetaldehyde obviously declined at the higher temperature while the others selectivity increased, which meant that side reactions of cross-aldol condensation were more conducive to occurrence than aldol condensation reaction [10,53]. To further reveal the rate-determining step, TPSR analysis was performed. For the ZnZr-S-1(hn-0.2) catalyst (Fig. 6b), the ethanol started to decline at 210 °C while the acetaldehyde and hydrogen obviously increased, indicating ethanol dehydrogenation occurrence. More hydrogen was detected than acetaldehyde, indicated that the formed acetaldehyde was rapidly involved in the subsequent aldol condensation reaction. Compared with ZnZr-S-1(hn-0.2) catalyst, Zr-S-1(hn-0.2) exhibited a weaker acetaldehyde peak at higher temperature, and the reduction of ethanol was significantly smaller (Fig. 6c). Furthermore, the initial butadiene formation temperature for ZnZr-S-1(hn-0.2) was much lower than that for Zr-S-1(hn-0.2). This result further verified that Zn species played an important role in the direct ETB reaction. No signals of acetaldehyde and crotyl alcohol were detected during the whole process, and only a very weak signal of crotonaldehyde appeared. Meanwhile, the peak of water obviously increased with increasing temperature, indicating the occurrence of dehydration reaction. In summary, these results revealed that the rate-determining step over ZnZr-S-1(hn-0.2) catalyst should be the aldol condensation (Fig. 6d), as acetaldehyde was the major intermediate product accumulated over the catalysts during the reaction process. The rapid reaction steps involved dehydration of acetaldehyde and crotyl alcohol (Fig. 6d), owing to the fact that acetaldehyde was not detected and only trace amounts of arotyl alcohol were detected during the reaction process.

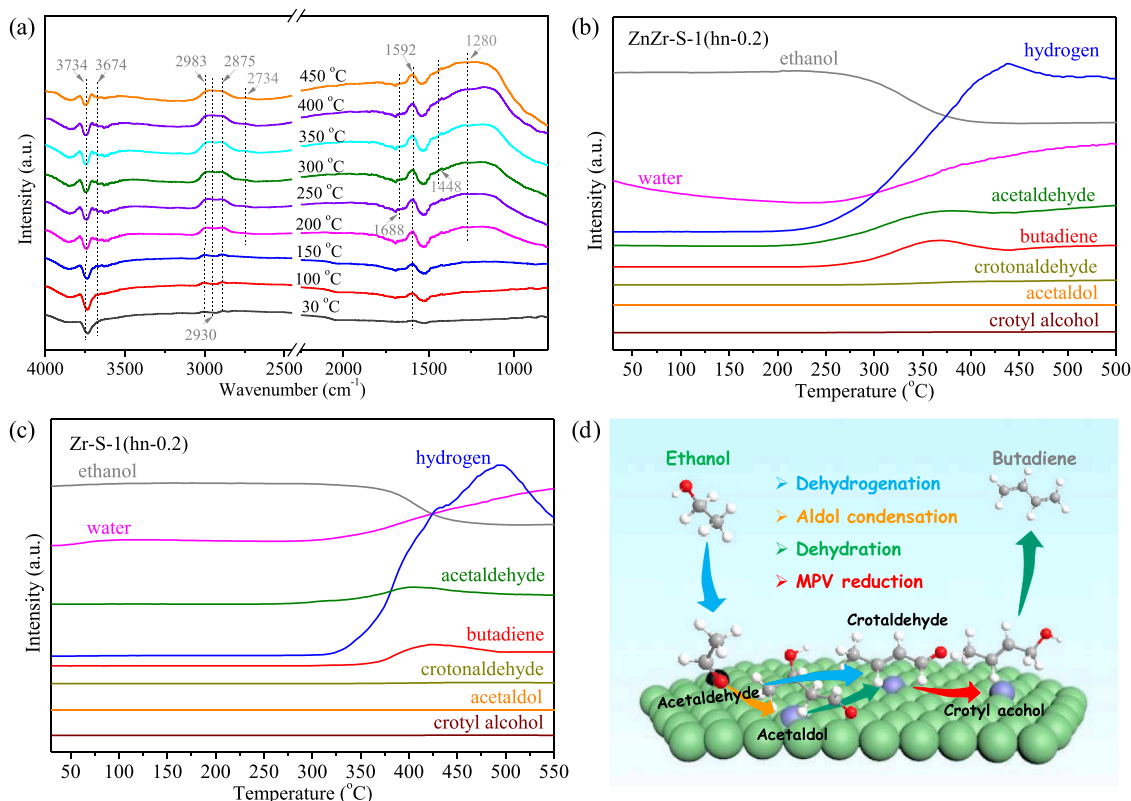
### 3.6. Catalyst stability

Fig. 7 compared the ethanol conversion and BD selectivity over ZnZr-S-1(hn-0.2) and ZnZr-S-1(mi-0.2) over reaction of 80 h. The ethanol conversion of ZnZr-S-1(hn-0.2) varied in a narrow range of 90.6–73.7% during 80 h on stream, whereas ZnZr-S-1(mi-0.2) exhibited a large drop from 84.7% to 59.9%. The coke deposition is the reason for the loss of activity, owing to the fact that the intermediate acetaldehyde and crotonaldehyde were transformed into heavier byproducts via cross-aldol condensation, reduction and dehydration, and the active centers of



**Fig. 5.** Effect of the reaction temperature (a) and WHSV (b) on catalytic performance of the direct ETB reaction over ZnZr-S-1(hn-0.2) catalyst. Reaction conditions: catalyst = 0.5 g, WHSV = 0.38 h<sup>-1</sup> (a), T = 350 °C (b), and TOS = 6 h. The butadiene, ethylene, acetaldehyde, diethyl ether, and 1-butanol were abbreviated as BD, C<sub>2</sub>=, AcH, DEE, and BuOH, respectively.





**Fig. 6.** Investigating the rate-determining steps. (a) TP-DRIFTS spectra obtained during the direct ETB conversion over ZnZr-S-1(hn-0.2) catalyst; (b) TPSR profiles in the direct ETB conversion over ZnZr-S-1(hn-0.2); (c) TPSR profiles in the direct ETB conversion over Zr-S-1(hn-0.2); (d) Schematic diagram of each detailed reaction step of direct ETB reaction.

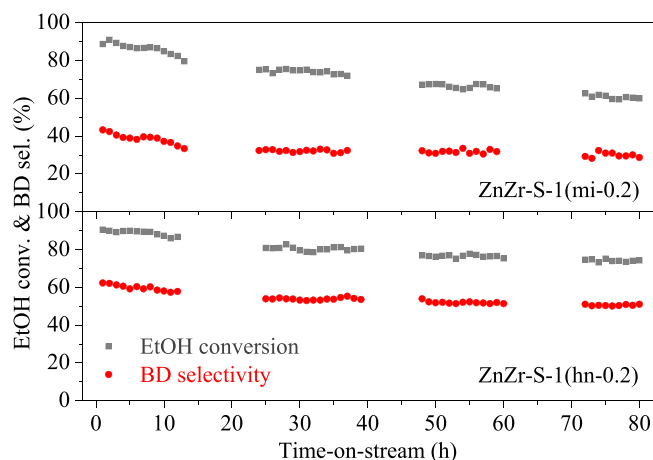


**Fig. 7.** Stability of ZnZr-S-1(mi-0.2) and ZnZr-S-1(hn-0.2) catalyst in the direct ETB reaction. Reaction conditions: catalyst = 0.5 g,  $T = 350\text{ }^{\circ}\text{C}$ , WHSV =  $0.23\text{ h}^{-1}$ , TOS = 80 h. The ethanol and butadiene were abbreviated as EtOH and BD.

catalysts were covered by these compounds, leading to catalyst deactivation [17,53]. Table S1 illustrates the catalytic stability investigated in this study compared to the stability of previously reported work under the corresponding reaction conditions. In comparison with other catalyst systems, we reported that hierarchical nano-sized ZnZr-S-1(hn-0.2) catalyst possessed superior catalytic stability and BD yield. Based on the above analysis on catalytic performance, the regeneration of ZnZr-S-1(mi-0.2) and ZnZr-S-1(hn-0.2) catalysts was conducted by calcination at  $500\text{ }^{\circ}\text{C}$  for 5 h in air atmosphere. The coke on spent catalysts could be burned off at this temperature. From the appearance, the color of

ZnZr-S-1(mi-0.2) and ZnZr-S-1(hn-0.2) changed from black back to white after regeneration (Fig. S9). It can be seen that the catalytic performances of spent catalysts were both thoroughly recovered after the first and second regenerations (Figs. S10 and S11). The initial catalytic performance of regenerated catalyst was almost the same as that of fresh catalyst. Thus, it can be seen that the catalytic performances of ZnZr-S-1(mi-0.2) and ZnZr-S-1(hn-0.2) catalysts can be restored to its original level after regeneration.

To further investigate the coke deposition phenomena, we characterized the spent catalyst via multiple technologies. Compared with fresh catalysts, the XRD pattern of the spent catalysts did not change significantly (Figs. S12 vs S1). We further analyzed the textural properties and TG of the spent ZnZr-S-1(mi-0.2) and ZnZr-S-1(hn-0.2) catalysts. The specific surface area of ZnZr-S-1(hn-0.2) displayed a low reduction compared to that of ZnZr-S-1(mi-0.2) ( $47\text{ vs }213\text{ m}^2\text{ g}^{-1}$ , in Table S7), owing to the fact that the pores of ZnZr-S-1(mi-0.2) were partially blocked by the coke deposition. In addition, the TG analysis identified that the spent ZnZr-S-1(hn-0.2) generated a much lower weight loss than that of ZnZr-S-1(mi-0.2) (Fig. S13). The binding energy of the fresh and spent catalysts Zn 2p and Zr 3d did not obviously change, but the peak intensity decreased (Figs. S14 and S15), this result revealed that the Zn and Zr species were partially covered by the coke deposition. These characterization results further proved that ZnZr-S-1(mi-0.2) had low mass transfer efficiency, which suppressed the diffusion of acetaldehyde, followed by the acetaldehyde and crotonaldehyde was transformed into heavier byproducts via cross-aldol condensation, reduction, and dehydration [15,56]. These compounds could further coverage the active centers, leading to catalyst deactivation [59]. On the other hand, ZnZr-S-1(hn-0.2) possessed a hierarchical nano-sized structure, which enhanced the diffusion of acetaldehyde and inhibited secondary reactions to form the coke deposition. Therefore, the excellent stability of the ZnZr-S-1(hn-0.2) catalyst should be attributed to the

hierarchical nano-sized structure, which provided highly accessible active centers and a short diffusion pathway.

#### 4. Conclusions

In this work, a series of hierarchical nano-sized ZnZr-Silicalite-1 multifunctional catalysts were fabricated by facile crystallization process and their catalytic performance for the selective conversion of ethanol to butadiene was investigated. The characterization results demonstrated that hierarchical nano-sized structure efficiently enhanced the synergy of multiple active centers to form more active centers and the ability of the resistance against carbon deposition. Meanwhile, Zn and Zr species efficiently modified acid-base properties, which could balance the various steps of the tandem reaction to achieve a high BD yield. A remarkable selectivity towards butadiene of 61.4% and ethanol conversion of 89.8% were obtained on hierarchical nano-sized ZnZr-Silicalite-1 multifunctional catalyst, especially it possessed good stability compared to the previously reported catalyst system.

#### CRediT Authorship Contribution Statement

**Kangzhou Wang:** Investigation, Methodology, Formal analysis, Writing – original draft, Visualization. **Weizhe Gao:** Data curation, Validation. **Fei Chen:** Data curation, Formal analysis. **Guangbo Liu:** Software, Validation. **Jinhu Wu:** Formal analysis, Software. **Na Liu:** Data curation, Investigation, Formal analysis. **Yugo Kawabata:** Data curation, Formal analysis. **Xiaoyu Guo:** Formal analysis, Software. **Yingluo He:** Conceptualization, Methodology, Writing – review & editing. **Peipei Zhang:** Conceptualization, Methodology, Writing – review & editing. **Guohui Yang:** Conceptualization, Methodology, Writing – review & editing. **Noritatsu Tsubaki:** Conceptualization, Methodology, Resources, Project administration, Supervision, Writing – review & editing.

#### Declaration of Competing Interest

The authors declare that they have no known competing financial interests or personal relationships that could have appeared to influence the work reported in this paper.

#### Acknowledgements

K. Wang acknowledges the financial support from China Scholarship Council (CSC, 201807550010).

#### Appendix A. Supporting information

Supplementary data associated with this article can be found in the online version at [doi:10.1016/j.apcatb.2021.120822](https://doi.org/10.1016/j.apcatb.2021.120822).

#### References

- [1] F. Cherubini, The biorefinery concept: using biomass instead of oil for producing energy and chemicals, *Energy Convers. Manag.* 51 (2010) 1412–1421, <https://doi.org/10.1016/j.enconman.2010.01.015>.
- [2] S. Sadhu, A.K. Bhowmick, Preparation and properties of nanocomposites based on acrylonitrile-butadiene rubber, styrene-butadiene rubber, and polybutadiene rubber, *J. Polym. Sci. Pol. Phys.* 42 (2004) 1573–1585, <https://doi.org/10.1002/polb.20036>.
- [3] M. Yang, F. You, Comparative techno-economic and environmental analysis of ethylene and propylene manufacturing from wet shale gas and naphtha, *Ind. Eng. Chem. Res.* 56 (2017) 4038–4051, <https://doi.org/10.1021/acs.iecr.7b00354>.
- [4] Y. Liu, F. Lu, Y. Tang, M. Liu, F.F. Tao, Y. Zhang, Effects of initial crystal structure of Fe<sub>2</sub>O<sub>3</sub> and Mn promoter on effective active phase for syngas to light olefins, *Appl. Catal. B Environ.* 261 (2020), 118219, <https://doi.org/10.1016/j.apcatb.2019.118219>.
- [5] E.V. Makshina, M. Dusselier, W. Janssens, J. Degreve, P.A. Jacobs, B.F. Sels, Review of old chemistry and new catalytic advances in the on-purpose synthesis of butadiene, *Chem. Soc. Rev.* 43 (2014) 7917–7953, <https://doi.org/10.1039/C4CS00105B>.
- [6] A.B. Diaz, A. Blandino, I. Caro, Value added products from fermentation of sugars derived from agro-food residues, *Trends Food Sci. Technol.* 71 (2018) 52–64, <https://doi.org/10.1016/j.tifs.2017.10.016>.
- [7] P. Lu, Q. Chen, G. Yang, L. Tan, X. Feng, J. Yao, Y. Yoneyama, N. Tsubaki, Space-confined self-regulation mechanism from a capsule catalyst to realize an ethanol direct synthesis strategy, *ACS Catal.* 10 (2020) 1366–1374, <https://doi.org/10.1021/acscatal.9b02891>.
- [8] T. Yan, W. Dai, G. Wu, S. Lang, M. Hunger, N. Guan, L. Li, Mechanistic insights into one-step catalytic conversion of ethanol to butadiene over bifunctional Zn-Y/beta zeolite, *ACS Catal.* 8 (2018) 2760–2773, <https://doi.org/10.1021/acscatal.8b00014>.
- [9] V.L. Sushkevich, I.I. Ivanova, Mechanistic study of ethanol conversion into butadiene over silver promoted zirconia catalysts, *Appl. Catal. B Environ.* 215 (2017) 36–49, <https://doi.org/10.1016/j.apcatb.2017.05.060>.
- [10] G. Pomalaza, P.A. Ponton, M. Capron, F. Dumeignil, Ethanol-to-butadiene: the reaction and its catalysts, *Catal. Sci. Technol.* 10 (2020) 4860–4911, <https://doi.org/10.1039/D0CY00784F>.
- [11] P.I. Kyriienko, O.V. Larina, S.O. Soloviev, S.M. Orlyk, Catalytic conversion of ethanol into 1,3-butadiene: achievement and prospects: a review, *Theor. Exp. Chem.* 56 (2020) 213–242, <https://doi.org/10.1007/s11237-020-09654-2>.
- [12] I.B. Samsudin, H. Zhang, S. Jaenicke, G.K. Chuah, Recent advances in catalysts for the conversion of ethanol to butadiene, *Chem. Asian J.* 15 (2020) 4199–4214, <https://doi.org/10.1002/asia.202001023>.
- [13] C. Wang, M. Zheng, X. Li, X. Li, T. Zhang, Catalytic conversion of ethanol into butadiene over high performance LiZnHf-MFI zeolite nanosheets, *Green Chem.* 21 (2019) 1006–1010, <https://doi.org/10.1039/C8GC03983F>.
- [14] O.V. Larina, N.D. Shcherban, P.I. Kyriienko, I.M. Remezovskiy, P.S. Yaremov, I. Khalakhan, G. Mali, S.O. Soloviev, S.M. Orlyk, S. Dzwigaj, Design of effective catalysts based on ZnLaZrSi oxide systems for obtaining 1,3-butadiene from aqueous ethanol, *ACS Sustain. Chem. Eng.* 8 (2020) 16600–16611, <https://doi.org/10.1021/acssuschemeng.0c05925>.
- [15] V.L. Dagle, M.D. Flake, T.L. Lemmon, J.S. Lopez, L. Kovarik, R.A. Dagle, Effect of the SiO<sub>2</sub> support on the catalytic performance of Ag/ZrO<sub>2</sub>/SiO<sub>2</sub> catalysts for the single-bed production of butadiene from ethanol, *Appl. Catal. B Environ.* 236 (2018) 576–587, <https://doi.org/10.1016/j.apcatb.2018.05.055>.
- [16] P.I. Kyriienko, O.V. Larina, S.O. Soloviev, S.M. Orlyk, C. Calers, S. Dzwigaj, Ethanol conversion into 1,3-butadiene by the Lebedev method over MTaSiBEA zeolites (M = Ag, Cu, Zn), *ACS Sustain. Chem. Eng.* 5 (2017) 2075–2083, <https://doi.org/10.1021/acssuschemeng.6b01728>.
- [17] T. Yan, L. Yang, W. Dai, C. Wang, G. Wu, N. Guan, M. Hunger, L. Li, On the deactivation mechanism of zeolite catalyst in ethanol to butadiene conversion, *J. Catal.* 367 (2018) 7–15, <https://doi.org/10.1016/j.jcat.2018.08.019>.
- [18] G. Pomalaza, G. Vofo, M. Capron, F. Dumeignil, ZnTa-TUD-1 as an easily prepared, highly efficient catalyst for the selective conversion of ethanol to 1,3-butadiene, *Green Chem.* 20 (2018) 3203–3209, <https://doi.org/10.1039/C8GC01211C>.
- [19] G. Pomalaza, P. Simon, A. Addad, M. Capron, F. Dumeignil, Properties and activity of Zn-Ta-TUD-1 in the Lebedev process, *Green Chem.* 22 (2020) 2558–2574, <https://doi.org/10.1039/D0GC00103A>.
- [20] X. Wang, Y. Men, J. Wang, S. Liu, Q. Song, M. Yang, The influence of zinc loadings on the selectivity control of bio-ethanol transformation over MgO-SiO<sub>2</sub> catalysts, *Appl. Catal. A Gen.* 598 (2020), 117565, <https://doi.org/10.1016/j.apcata.2020.117565>.
- [21] W. Dai, S. Zhang, Z. Yu, T. Yan, G. Wu, N. Guan, L. Li, Zeolite structural confinement effects enhance one-pot catalytic conversion of ethanol to butadiene, *ACS Catal.* 7 (2017) 3703–3706, <https://doi.org/10.1021/acscatal.7b00433>.
- [22] X. Yang, Y. Liu, X. Li, J. Ren, L. Zhou, T. Lu, Y. Su, Synthesis of Sn-containing nanosized beta zeolite as efficient catalyst for transformation of glucose to methyl lactate, *ACS Sustain. Chem. Eng.* 6 (2018) 8256–8265, <https://doi.org/10.1021/acssuschemeng.8b00177>.
- [23] Y. Shi, Q. Zhou, Z. Qin, Z. Wu, W. Jiao, M. Dong, W. Fan, J. Wang, Hierarchically structured Pt/K-Beta zeolites for the catalytic conversion of n-heptane to aromatics, *Microporous Mesoporous Mater.* 324 (2021), 111308, <https://doi.org/10.1016/j.micromeso.2021.111308>.
- [24] A. Parulkar, R. Joshi, N. Deshpande, N.A. Brunelli, Synthesis and catalytic testing of Lewis acidic nano-MFI zeolites for the epoxide ring opening reaction with alcohol, *Appl. Catal. A Gen.* 566 (2018) 25–32, <https://doi.org/10.1016/j.apcata.2018.08.018>.
- [25] T. Weissenberger, B. Reiprich, A.G. Machoke, K. Klühspies, J. Bauer, R. Dotzel, J. L. Casci, W. Schiewer, Hierarchical MFI type zeolites with intracrystalline macropores: the effect of the macropore size on the deactivation behavior in the MTO reaction, *Catal. Sci. Technol.* 9 (2019) 3259–3269, <https://doi.org/10.1039/C9CY00368A>.
- [26] Y.Q. Deng, S.F. Yin, C.T. Au, Preparation of nano-sized silicalite-1 and its application in vapor-phase Beckmann rearrangement of cyclohexanone oxime, *Ind. Eng. Chem. Res.* 51 (2012) 9492–9499, <https://doi.org/10.1021/ie3001277>.
- [27] V. Smeets, E.M. Gaigneaux, D.P. Debecker, Hierarchical micro-/macroporous TS-1 zeolite epoxidation catalyst prepared by stream assisted crystallization, *Microporous Mesoporous Mater.* 293 (2020), 109801, <https://doi.org/10.1016/j.micromeso.2019.109801>.
- [28] Y. Tian, J. Qi, W. Zhang, Q. Cai, X. Jiang, Facile, one-pot synthesis, and antibacterial activity of mesoporous silica nanoparticles decorated with well-dispersed silver nanoparticles, *ACS Appl. Mater. Interfaces* 6 (2014) 12038–12045, <https://doi.org/10.1021/am5026424>.
- [29] C.A. Emeis, Determination of integrated molar extinction coefficient for infrared absorption bands of pyridine adsorbed on solid acid catalysts, *J. Catal.* 141 (1993) 347–354, <https://doi.org/10.1006/jcat.1993.1145>.

- [30] Y. Zhu, G. Chuah, S. Jaenicke, Chemo- and regioselective Meerwein-Ponndorf-Verley and Oppenauer reactions catalyzed by Al-free Zr-zeolite beta, *J. Catal.* 227 (2004) 1–10, <https://doi.org/10.1016/j.jcat.2004.05.037>.
- [31] C. Thunyaratchatanon, A. Luengnaruemitchai, T. Chaisuwan, N. Chollacoop, S. Y. Chen, Y. Yoshimura, Synthesis and characterization of Zr incorporation into highly ordered mesostructured SBA-15 material and its performance for CO<sub>2</sub> adsorption, *Microporous Mesoporous Mater.* 253 (2017) 18–28, <https://doi.org/10.1016/j.micromeso.2017.06.015>.
- [32] W. Gao, C.C. Amoo, G. Zhang, M. Javed, B. Mazonde, C. Lu, R. Yang, C. Xing, N. Tsubaki, Insight into solvent-free synthesis of MOR zeolite and its laboratory scale production, *Microporous Mesoporous Mater.* 280 (2019) 187–194, <https://doi.org/10.1016/j.micromeso.2019.01.041>.
- [33] F. Ramezani, R. Zare-Dorabeh, Simultaneous ultrasonic-assisted removal of malachite green and methylene blue from aqueous solution by Zr-SBA-15, *Polyhedron* 166 (2019) 153–161, <https://doi.org/10.1016/j.poly.2019.03.033>.
- [34] D. Lesthaeghe, P. Vansteenkiste, T. Verstraelen, A. Ghysels, C.E. Kirschhock, J. A. Martens, V.V. Speybroeck, M. Waroquier, MFI fingerprint: how pentasil-induced IR bands shift during zeolite nanogrowth, *J. Phys. Chem. C* 112 (2008) 9186–9191, <https://doi.org/10.1021/jp711550s>.
- [35] G. Greczynski, L. Hultman, Reliable determination of chemical state in x-ray photoelectron spectroscopy based on sample-work-function referencing to adventitious carbon: resolving the myth of apparent constant binding energy of the C 1s peak, *Appl. Surf. Sci.* 451 (2018) 99–103, <https://doi.org/10.1016/j.apsusc.2018.04.226>.
- [36] G. Greczynski, L. Hultman, X-ray photoelectron spectroscopy: towards reliable binding energy referencing, *Prog. Mater. Sci.* 107 (2020), 100591, <https://doi.org/10.1016/j.pmatsci.2019.100591>.
- [37] M. Jacquemin, M.J. Genet, E.M. Gaigneaux, D.P. Debecker, Calibration of the X-Ray photoelectron spectroscopy binding energy scale for the characterization of heterogeneous catalysts: is everything really under control? *ChemPhysChem* 14 (2013) 3618–3626, <https://doi.org/10.1002/cphc.201300411>.
- [38] A.V. Boryakov, S.I. Surodin, R.N. Kryukov, D.E. Nikolichev, S. Yu. Zubkov, Spectral fit refinement in XPS analysis technique and its practical applications, *J. Electron. Spectrosc. Relat. Phenom.* 229 (2018) 132–140, <https://doi.org/10.1016/j.elspec.2017.11.004>.
- [39] K. Wang, X. Peng, X. Gao, Y. Araki, H. Zhao, J. Liang, L. Xiao, J. Chen, G. Liu, J. Wu, G. Yang, N. Tsubaki, Insights into the synergistic effect of active centers over ZnMg/SBA-15 catalysts in direct synthesis of butadiene from ethanol, *React. Chem. Eng.* 6 (2021) 548–558, <https://doi.org/10.1039/D0RE00449A>.
- [40] B. Rakshe, V. Ramaswamy, S.G. Hegde, R. Vetrivel, A.V. Ramaswamy, Crystalline, microporous zirconium silicates with MFI structure, *Catal. Lett.* 45 (1997) 41–50, <https://doi.org/10.1023/A:1019078520445>.
- [41] Y.S. Ko, W.S. Ahn, Synthesis and characterization of zirconium silicalite-1, *Korean J. Chem. Eng.* 15 (1998) 423–428, <https://doi.org/10.1007/BF02697133>.
- [42] R. Fricke, H. Kosslick, V.A. Tuan, I. Grohmann, W. Pilz, W. Storek, G. Walther, Study on the isomorphous substitution of silicon by tetravalent elements (Zr, Ge, Ti) in the framework of MFI type zeolites, *Stud. Surf. Sci. Catal.* 83 (1994) 57–66, [https://doi.org/10.1016/S0167-2991\(08\)63242-5](https://doi.org/10.1016/S0167-2991(08)63242-5).
- [43] Z. Zhao, Y. Liu, H. Wu, X. Li, M. He, P. Wu, Hydrothermal synthesis of mesoporous zirconosilicate with enhanced textural and catalytic properties with the aid of amphiphilic organosilane, *Microporous Mesoporous Mater.* 123 (2009) 324–330, <https://doi.org/10.1016/j.micromeso.2009.04.018>.
- [44] K. Wang, S. Fan, J. Zhang, Q. Ma, W. Zhang, T.S. Zhao, Effects of synergy between Cr<sub>2</sub>O<sub>3</sub> and hierarchical HZSM-5 on transformation of LPG toward propylene and ethylene, *Fuel Process. Technol.* 179 (2018) 53–59, <https://doi.org/10.1016/j.fuproc.2018.06.014>.
- [45] T. Onfroy, G. Clet, S. Bukallah, D. Hercules, M. Houalla, Development of the acidity of zirconia-supported niobia catalysts, *Catal. Lett.* 89 (2003) 15–19, <https://doi.org/10.1023/A:1024717505705>.
- [46] K. Wang, J. Zhang, S. Fan, X. Peng, N. Tsubaki, T.S. Zhao, Transformation of LPG to light olefins on composite HZSM-5/SAPO-5, *New J. Chem.* 45 (2021) 4860–4866, <https://doi.org/10.1039/D1NJ00018G>.
- [47] Y. Liu, C. Xia, Q. Wang, L. Zhang, A. Huang, M. Ke, Z. Song, Direct dehydrogenation of isobutane to isobutene over Zn-doped ZrO<sub>2</sub> metal oxide heterogeneous catalysts, *Catal. Sci. Technol.* 8 (2018) 4916–4924, <https://doi.org/10.1039/C8CY01420E>.
- [48] H. Krishna, M.O. Haus, R. Palkovits, Basic silica catalysts for the efficient dehydration of biomass-derived compounds – elucidating structure-activity relationships for Na<sub>2</sub>O/SiO<sub>2</sub>-type materials, *Appl. Catal. B Environ.* 286 (2021), 119933, <https://doi.org/10.1016/j.apcatb.2021.119933>.
- [49] C. Angelici, M.E.Z. Velthoen, B.M. Weckhuysen, P.C.A. Bruijninx, Influence of acid-base properties on the Lebedev ethanol-to-butadiene process catalyzed by SiO<sub>2</sub>-MgO materials, *Catal. Sci. Technol.* 5 (2015) 2869–2879, <https://doi.org/10.1039/C5CY00200A>.
- [50] K. Wang, L. Guo, W. Gao, B. Zhang, H. Zhao, J. Liang, N. Liu, Y. He, P. Zhang, G. Yang, N. Tsubaki, One-pot hydrothermal synthesis of multifunctional ZnZrTUD-1 catalysts for highly efficient direct synthesis of butadiene from ethanol, *ACS Sustain. Chem. Eng.* 9 (2021) 10569–10578, <https://doi.org/10.1021/acssuschemeng.1c02630>.
- [51] T. Miyazawa, Y. Tanabe, I. Nakamura, Y. Shinke, M. Hiza, Y.K. Choe, T. Fujitani, Fundamental roles of ZnO and ZrO<sub>2</sub> in the conversion of ethanol to 1,3-butadiene over ZnO-ZrO<sub>2</sub>/SiO<sub>2</sub>, *Catal. Sci. Technol.* 10 (2020) 7531–7541, <https://doi.org/10.1039/D0CY01453B>.
- [52] V.L. Sushkevich, I.I. Ivanova, E. Taarning, Ethanol conversion into butadiene over Zr-containing molecular sieves doped with silver, *Green Chem.* 17 (2015) 2552–2559, <https://doi.org/10.1039/C4GC02202E>.
- [53] V.L. Sushkevich, I.I. Ivanova, V.V. Ordonsky, E. Taarning, Design of a metal-promoted oxide catalyst for the selective synthesis of butadiene from ethanol, *ChemSusChem* 7 (2014) 2527–2536, <https://doi.org/10.1002/cssc.201402346>.
- [54] M. Zhang, M. Gao, J. Chen, Y. Yu, Study on key step of 1,3-butadiene formation from ethanol on MgO/SiO<sub>2</sub>, *RSC Adv.* 5 (2015) 25959–25966, <https://doi.org/10.1039/C4RA17070A>.
- [55] X. Zhang, R. Wang, X. Yang, F. Zhang, Comparison of four catalysts in the catalytic dehydration of ethanol to ethylene, *Microporous Mesoporous Mater.* 116 (2008) 210–215, <https://doi.org/10.1016/j.micromeso.2008.04.004>.
- [56] X. Huang, Y. Men, J. Wang, W. An, Y. Wang, Highly active and selective binary MgO-SiO<sub>2</sub> catalysts for the production of 1,3-butadiene from ethanol, *Catal. Sci. Technol.* 7 (2017) 168–180, <https://doi.org/10.1039/C6CY02091G>.
- [57] T. Moteki, A.T. Rowley, D.T. Bregante, D.W. Flaherty, Formation pathways toward 2- and 4-methylbenzaldehyde via sequential reactions from acetaldehyde over hydroxyapatite catalyst, *ChemCatChem* 9 (2017) 1–10, <https://doi.org/10.1002/cctc.201700151>.
- [58] A.K.P. Mann, Z. Wu, F.C. Calaza, S.H. Overbury, Adsorption and reaction of acetaldehyde on shape-controlled CeO<sub>2</sub> nanocrystals: elucidation of structure-function relationship, *ACS Catal.* 4 (2014) 2437–2448, <https://doi.org/10.1021/cs500611g>.
- [59] A. Chieriegato, J. Velasquez Ochoa, C. Bandinelli, G. Fornasari, F. Cavani, M. Mella, On the chemistry of ethanol on basic oxides: revising mechanisms and intermediates in the Lebedev and Guerbet reactions, *ChemSusChem* 8 (2015) 377–388, <https://doi.org/10.1002/cssc.201402632>.